



Is it meaningful to quantify vacancy concentrations of nanolamellar (Ti,Al)N thin films based on laser-assisted atom probe data?

Marcus Hans^{a,*}, Michael Tkadletz^b, Daniel Primetzhofer^c, Helene Waldl^d, Maximilian Schiester^e, Matthias Bartosik^b, Christoph Czettl^f, Nina Schalk^d, Christian Mitterer^b, Jochen M. Schneider^a

^a Materials Chemistry, RWTH Aachen University, Kopernikusstraße 10, 52074 Aachen, Germany

^b Department of Materials Science, Montanuniversität Leoben, Franz-Josef-Straße 18, 8700 Leoben, Austria

^c Department of Physics and Astronomy, Uppsala University, Lägerhyddsvägen 1, 75120 Uppsala, Sweden

^d Christian Doppler Laboratory for Advanced Coated Cutting Tools, Montanuniversität Leoben, Franz-Josef-Straße 18, 8700 Leoben, Austria

^e Materials Center Leoben Forschung GmbH, Roseggerstraße 12, 8700 Leoben, Austria

^f Ceratizit Austria GmbH, Metallwerk-Plansee-Straße 71, 6600 Reutte, Austria

ARTICLE INFO

Keywords:

Transition metal nitrides
Atom probe tomography
Defects
Accuracy

ABSTRACT

Recently, it was proposed to quantify vacancy concentrations based on laser-assisted atom probe tomography (APT) data for a (Ti,Al)N film with a nanolamellar architecture, grown by chemical vapor deposition. To determine, whether vacancy concentrations can be reliably estimated based on APT data, we systematically compare measurements with an ultraviolet (UV) as well as a green laser to ion beam analysis data. First, monolithic TiN and AlN films, which are stoichiometric within the measurement uncertainties of ion beam analysis, are investigated. In case of TiN an electric field strength of 39.4 V nm^{-1} and a nitrogen content of 49.0 at.%, consistent with ion beam analysis data, is obtained with both lasers, when using pulse energies of 5 pJ (UV laser) and 0.1 nJ (green laser). However, significant differences can be observed for monolithic AlN as nitrogen contents from 41.9 to 35.8 at.% and 48.4 to 41.4 at.% are measured, depending on variations of the pulse energies of the UV and green laser, respectively. In order to mimic a nanolamellar architecture for correlative compositional analysis by ion beam analysis and laser-assisted APT, a TiN/AlN/TiN trilayer film is synthesized and significant deviations with respect to the nitrogen content are evident for the AlN layer. While the average nitrogen concentration from ion beam analysis is 51 at.%, nitrogen contents from laser-assisted APT data are only 38 at.% (UV laser) or 41 at.% (green laser). Hence, the nitrogen content of the AlN layer is underestimated from laser-assisted APT data by at least 10 and up to 13 at.% and this significant discrepancy cannot be explained by the measurement uncertainties. Thus, the here presented data emphasize that it is not meaningful to quantify vacancy concentrations of nanolamellar (Ti,Al)N thin films solely based on atom probe data, since the measurement accuracy depends on the field evaporation conditions.

1. Introduction

Atom probe tomography (APT) is a powerful characterization technique for identifying composition variations at the nanometer scale, as spatially-resolved imaging of field evaporated atoms in three dimensions is enabled by combination of mass spectrometry and projection microscopy. The measurement of compositional variations at the nanometer scale is highly-relevant for understanding the stability of hard coatings, e.g. spinodal decomposition and nucleation and growth

of wurtzite AlN in transition metal aluminum nitrides [1–4], and the first atom probe dataset from (Ti,Al)N films was published in 2009 by Rachbauer et al. [5]. As the electrical conductivity of nitrides is limited, field evaporation from needle-shaped specimens [6] is typically assisted by an electric field coupled with thermal pulsing through a femtosecond laser [7]. After eventual field evaporation of single atoms, ionization occurs in the vicinity of the surface electric field at the specimen [8] and these ions are then captured with a position-sensitive detection system.

Within the last decade the availability of commercial atom probe

* Corresponding author.

E-mail address: hans@mch.rwth-aachen.de (M. Hans).

<https://doi.org/10.1016/j.surfcoat.2023.130020>

Received 23 June 2023; Received in revised form 23 August 2023; Accepted 12 September 2023

Available online 14 September 2023

0257-8972/© 2023 The Authors. Published by Elsevier B.V. This is an open access article under the CC BY license (<http://creativecommons.org/licenses/by/4.0/>).

systems for research groups associated with the hard coating community has increased. While there are currently 52 publications with atom probe data from hard nitride films,¹ a significant increase has to be expected in the future. Generally, to avoid misinterpretation of data, awareness for the technique-inherent limitations is required. The consequences of ignoring such limitations is currently debated for X-ray photoelectron spectroscopy data as half a century of data (>10,000 papers published annually nowadays) appears questionable due to incorrect referencing of the binding energy [9]. Recent reports on limitations of APT emphasize the limited effective spatial resolution to >1 nm for the analysis of small particles and solute clusters [10] and that lateral neighborhood relationships are typically affected by the field evaporation process [11]. Moreover, a large amount of publications on systematic compositional discrepancies in GaN [12–17] as well as (Al, Ga)N [18,19] is available.

The limited measurement accuracy of APT for nitrides seems not to be recognized by the hard coating community, yet. Recently, vacancy concentrations were published for a (Ti,Al)N film with a nanolamellar architecture, grown by chemical vapor deposition (CVD). Based on quantitative composition data from laser-assisted APT, Qiu et al. concluded that titanium-rich volumes exhibit up to 12 % metal vacancies and aluminum-rich volumes exhibit up to 36 % nitrogen vacancies [20]. Though it appears reasonable that metal and nitrogen vacancies govern nitrogen overstoichiometry and understoichiometry [21], thereby affecting the decomposition kinetics [22,23], the meaningfulness of quantifying vacancy concentrations solely based on laser-assisted APT data has to be questioned.

We have demonstrated that the measurement accuracy of laser-assisted APT for (Ti,Al)N is governed by the electric field strength [24]. The electric field strength is correlated with the probability of post-ionization and can be estimated based on charge state ratios [25], which are extracted from measured mass spectra. Using $\text{Ti}^{3+}/\text{Ti}^{2+}$ and $\text{Al}^{2+}/\text{Al}^{+}$ charge state ratios, electric field strengths on the order of 40 V nm^{-1} and $<30 \text{ V nm}^{-1}$, respectively, have been obtained for titanium and aluminum in (Ti,Al)N [26]. Hence, the field evaporation of aluminum-rich volumes requires a significantly lower electric field strength than titanium-rich volumes. Based on the comparison with ion beam analysis data, which provided a nitrogen concentration of $50.5 \pm 1.3 \text{ at.}\%$, underestimation of the nitrogen content by laser-assisted APT from 4.1 at. % at 10 pJ laser pulse energy to 11.4 at. % at 200 pJ laser pulse energy was observed and the aluminum content was overestimated by 3.0 and 8.8 at. %, respectively [24]. Concomitantly, the electric field strength, estimated from the $\text{Al}^{2+}/\text{Al}^{+}$ charge state ratio, was reduced from 28 to 25 V nm^{-1} , when the laser pulse energy was increased from 10 to 200 pJ. Thus, a reduction of electric field strength by 3 V nm^{-1} causes nitrogen underestimation by >7 at. % and aluminum overestimation by >5 at. %. The correlation of lower nitrogen contents with aluminum-rich volumes can be also found in numerous publications of different transition metal aluminum nitrides [3–5,27–32].

In order to answer the question raised in the title of this work, we mimic a nanolamellar CVD-(Ti,Al)N film through synthesis of a trilayer architecture of TiN/AlN/TiN with nominal thickness of ~40 nm per layer. Such a trilayer architecture exhibits defined, straight interfaces and thereby enables the correlation of compositions from ion beam analysis and laser-assisted APT data. The effect of the laser type on the measurement accuracy is examined through employment of two local electrode atom probes with an ultraviolet (UV) as well as a green laser. The here presented data emphasize that it is not meaningful to quantify vacancy concentrations of (Ti,Al)N thin films solely based on APT data.

2. Experimental details

2.1. Film growth

Three sets of thin films were produced as described in the following.

- Nanolamellar CVD-(Ti,Al)N was synthesized on a cemented carbide cutting insert in an industrial Sucotec SCT 600TH hot wall reactor at 790°C . TiCl_4 , AlCl_3 , NH_3 , H_2 , N_2 and Ar precursors were used at a deposition pressure of 9400 Pa and the central gas feed was rotated at a speed of 4 min^{-1} . Further details can be found in [33].
- Monolithic TiN (cubic phase, space group $Fm\bar{3}m$) and AlN (wurtzite phase, space group $P6_3mc$) films were grown on silicon (100) substrates using physical vapor deposition (PVD) within an industrial CemeCon CC800/9 system. Titanium (>99.5 % purity) and aluminum (>99.5 % purity) targets from Plansee Composite Materials GmbH were used and the minimum target-to-substrate distance during two-fold substrate rotation was 7.6 cm. The growth temperature of 550°C was achieved with radiation heaters. Argon and nitrogen flows of 200 and 80 sccm were used, resulting in a reactive gas mixture of $\text{N}_2/(\text{Ar}+\text{N}_2) = 0.3$ and the deposition pressure was 0.6 Pa. DC as well as pulsed DC magnetron sputtering were employed for the titanium and aluminum targets with time-average powers of $P_{\text{Ti}} = 7 \text{ kW}$ and $P_{\text{Al}} = 7 \text{ kW}$ (50 kHz frequency), respectively.
- The TiN/AlN/TiN trilayer film was synthesized by unbalanced reactive magnetron sputtering in a laboratory AJA International ATC 1800 system. Layers with nominal thickness of ~40 nm were grown on silicon (100) substrates, which were ultrasonically pre-cleaned in acetone and ethanol for 5 min each, mounted on the substrate holder and transferred into the deposition system. The deposition chamber was evacuated to a base pressure below $3 \times 10^{-4} \text{ Pa}$. The substrates were then thermally cleaned at 350°C for 20 min and the titanium target (75 mm diameter, 99.995 % purity, Kurt J. Lesker) and the aluminum target (75 mm diameter, 99.99 % purity, Kurt J. Lesker) were sputter-cleaned behind closed shutters. The trilayer was grown at the same temperature in a mixed argon/nitrogen atmosphere. The argon gas flow was set to 14 sccm and the nitrogen gas flow to 6 sccm, corresponding to a $\text{N}_2/(\text{Ar}+\text{N}_2)$ ratio of 0.3 at a total deposition pressure of 0.2 Pa. The magnetrons were powered in pulsed DC mode (100 kHz pulse frequency, 1 μs pause duration). A time-average power of 350 W was applied to the titanium target and 500 W to the aluminum target, resulting in deposition rates of ~5 and ~18 nm min^{-1} for TiN and AlN, respectively. During film growth, a DC bias voltage of -70 V was applied to the substrates to obtain a dense film morphology. The substrate holder was continuously rotated at a frequency of ~0.5 Hz during the film synthesis.

2.2. Ion beam analysis

Ion beam analysis has been carried out at the Tandem Laboratory of Uppsala University [34]. Composition depth profiling was done by time-of-flight elastic recoil detection analysis (ToF-ERDA) using $36 \text{ MeV } ^{127}\text{I}^{8+}$ primary ions. The ion beam was directed onto the sample at an angle of 67.5° with respect to the surface normal and time-energy coincidence spectra were obtained at an angle of 45° with respect to the primary beam. A gas detector was used [35] and further details concerning the detection system are available in [36]. Sources of uncertainty for ToF-ERDA are the detection efficiency <1, in particular for light recoils which can be calibrated from beams of the specimen of interest and thin targets, as well as potential uncertainties from the specific energy loss of primary ions and recoil species [23]. In order to further minimize these uncertainties [37], ToF-ERDA was combined

¹ Based on a search query of TITLE-ABS-KEY (“atom probe”) AND (“coating” OR “thin film”) AND (“nitride” OR “TiAlN”)) at Scopus on 23 August 2023.

with Rutherford backscattering spectrometry (RBS) using 2 MeV $^4\text{He}^+$ ions, which were detected at a scattering angle of 170° . Data analysis was done with CONTES [38] and SIMNRA [39]. The total measurement uncertainty was 3 % relative from the deduced values. The densities of 5.34 g cm^{-3} for TiN and 3.20 g cm^{-3} for AlN as well as the atomic masses of titanium, aluminum and nitrogen were used to estimate the depth values of the ToF-ERDA profiles in nanometers for the monolithic films. In case of the depth profile from the TiN/AlN/TiN trilayer, complementary thickness measurements based on electron microscopy (see Section 2.4) were used.

2.3. X-ray diffraction

X-ray diffraction of the CVD-(Ti,Al)N as well as the monolithic TiN and AlN films was carried out using a Bruker D8 Advance diffractometer equipped with a Cu X-ray tube and parallel beam optics (i.e. a Göbel mirror on the primary and a 0.12° equatorial soller collimator on the secondary side). Scans were performed in grazing incidence geometry at an incidence angle of 2° and covering a 2θ range of 30 to 80° , using a step size of 0.02° and a dwell time of 1.2 s. Diffractograms of the CVD-(Ti,Al)N as well as monolithic TiN and AlN films are shown in Fig. S11 of the Supplementary information, while the crystalline domains of the TiN/AlN/TiN trilayer were too small for XRD characterization. The CVD-(Ti,Al)N consists predominantly of the cubic phase and only traces of wurtzite AlN are observable. Monolithic TiN and AlN films exhibit cubic and wurtzite single-phase formation, respectively.

2.4. Electron microscopy

The microstructure and thickness of the monolithic films as well as the TiN/AlN/TiN trilayer were investigated by scanning transmission electron microscopy (STEM). Cross-sectional thin lamellae were prepared by focused ion beam (FIB) techniques using a FEI Helios Nanolab 660 dual-beam microscope with gallium ions. Micrographs were acquired with a STEM III detector in bright field mode at 30 kV acceleration voltage. Moreover, electron backscatter diffraction (EBSD) was employed to identify a grain with (001) orientation in the CVD-(Ti,Al)N film for site-specific specimen preparation. An EDAX system with a Hikari camera was used at 10 kV acceleration voltage, 20 nA current and the step size was 50 nm. Atom probe specimens were prepared by FIB techniques according to a standard protocol [40] in a FEI Versa 3D and the above mentioned FEI Helios Nanolab 660 dual-beam microscope. Final annular milling of the needle-shaped specimens was done at low voltage $\leq 5 \text{ kV}$ to reduce the gallium contamination.

2.5. Atom probe tomography

Local composition measurements at the nanometer scale were done by laser-assisted atom probe tomography using two local electrode atom probes: a CAMECA LEAP 4000X HR (UV laser, $\lambda = 355 \text{ nm}$) and a CAMECA LEAP 3000X HR (green laser, $\lambda = 532 \text{ nm}$). These systems will be referred to according to the laser type (UV, green) in the following. Field evaporation of the three sets of films described above was assisted by laser pulsing. Besides constant base temperature of 60 K, the following parameters were used:

- (i) The nanolamellar CVD-(Ti,Al)N specimen with (001) orientation was measured in the atom probe with the UV laser at constant laser pulse energy of 30 pJ, 125 kHz frequency and 0.5 % detection rate. 1 million ions were detected before fracture of the specimen.
- (ii) Monolithic TiN and AlN films were measured in both systems. The pulse energy of the UV laser was varied from 5 to 10, 30, 50, 30, 10 and 5 pJ within a single measurement, while the laser pulse frequency was 200 kHz and the detection rate was 1.0 %. Similarly, the pulse energy of the green laser was varied from 0.1

to 0.5, 1.0, 1.5 and 2.0 nJ within a single measurement at 250 kHz laser pulse frequency and 0.5 % detection rate. 5×10^6 ions were collected per pulse energy in both systems.

- (iii) The TiN/AlN/TiN trilayer film was also characterized in both atom probes. Based on the findings for the monolithic films a pulse energy of 10 pJ was used for the UV laser and the laser pulse frequency and detection rate were 125 kHz and 0.5 %. Measurements with the green laser were carried out with identical parameters as employed by Qiu et al. [20]: 0.5 nJ, 200 kHz and an average detection rate of 0.2 %.

Data analysis was carried out with AP Suite 6.1 and IVAS 3.6.14. Ranging of the mass spectra was intended to minimize the contribution of thermal tails. For each peak the mass-to-charge state ratio of the maximum intensity was identified (e.g. 13.494 Da for Al^{2+}) and compared to the peak onset from the background (e.g. 13.450 Da for Al^{2+}). The range was then defined symmetrically by the difference of these mass-to-charge state ratios (e.g. 13.450 to 13.538). This symmetric ranging approach was compared systematically to ranging including the thermal tails for monolithic TiN and AlN films, measured with the UV laser. Average isotope ratios of nitrogen and titanium as well as quantified compositions for different laser pulse energies are provided in Tables S11 to S14 in the Supplementary information. It can be learned that the ranging approach has no significant effect on the quantification as the compositional deviations are within the precision of laser-assisted APT ($\pm 1 \text{ at.}\%$) [26].

3. Results and discussion

3.1. Composition of nanolamellar CVD-(Ti,Al)N from APT with UV laser

The film surface of the CVD-(Ti,Al)N film has been imaged with backscattered electrons in order to visualize grains and grain boundaries (Fig. 1a). EBSD mapping provides evidence for the formation of a polycrystalline film, composed of grains with sizes in the range of 200 nm to $1 \mu\text{m}$ (Fig. 1b). A site-specific lift-out from a grain with orientation close to (001) has been carried out since the nanolamellae in such a grain are arranged parallel to the surface as can be seen by STEM imaging of the atom probe specimen [41] before transfer to the atom probe microscope (Fig. 1c). Atom probe measurements were carried out with the UV laser and the reconstruction of atomic positions from a volume of $\sim 30 \times 30 \times 100 \text{ nm}^3$ provides evidence for composition modulations (Fig. 1d). The composition profile, obtained from a cylinder with 5 nm diameter, reveals nitrogen variations, depending on the metal sublattice (Fig. 1e): titanium- and aluminum-rich nanolamellae exhibit an average nitrogen content of 42 ± 4 and $34 \pm 3 \text{ at.}\%$, respectively. Moreover, mass spectra of titanium and aluminum-rich nanolamellae have been obtained from cuboid volumes of $1 \times 1 \times 25 \text{ nm}^3$ (Fig. 1f, volume indicated by solid lines in Fig. 1d). It is evident that for the aluminum-rich nanolamella the aluminum signal is increased significantly more than the nitrogen signal.

However, the composition of individual nanolamellae from CVD-(Ti,Al)N films cannot be resolved by ion beam analysis, as the measurement spot size during ToF-ERDA and RBS is $\sim 3 \times 1$ and $\sim 1 \times 1 \text{ mm}^2$, respectively, thus covering millions of grains with different orientations (see Fig. 1b). Since the nanolamellae from CVD-(Ti,Al)N films are titanium-rich and aluminum-rich, a systematic comparison of nitrogen quantification using laser-assisted APT with the UV and green laser has been carried out for monolithic TiN and AlN in the following.

3.2. Effect of laser type on the quantification of monolithic films

The composition of monolithic TiN and AlN thin films has been quantified through ion beam analysis and ToF-ERDA depth profiles, supported by RBS data, are presented in Fig. 2a and b, respectively. The TiN film exhibits a homogeneous composition profile and, neglecting the

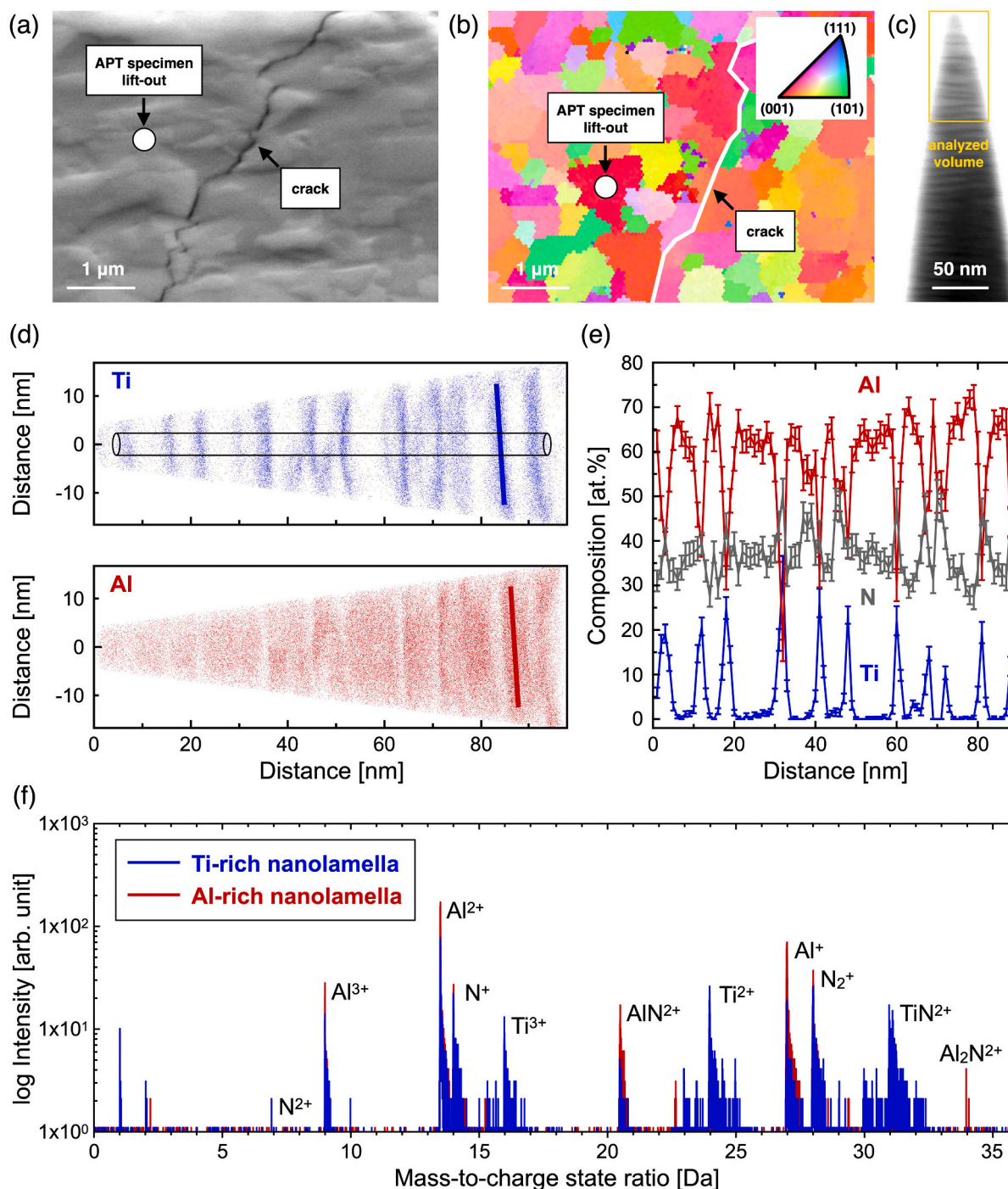


Fig. 1. Composition and mass spectrum analysis of CVD-(Ti,Al)N. (a) Backscattered electron image of the film surface at a tilt angle of 52°. The crack formation is caused by thermal stresses during cooling down after film deposition and the crack is highlighted as reference for the (b) inverse pole figure, obtained by EBSD mapping. An atom probe specimen was prepared from a grain with (001) orientation (highlighted in (a) and (b)). (c) STEM imaging of the atom probe specimen before transfer to the atom probe microscope [41]. (d) Reconstruction of atomic positions of elemental titanium and aluminum ions, measured with the UV laser. The analyzed total volume is indicated in (c). (e) Composition profile from the cylindrical volume (5 nm diameter) shown in (d). (f) Mass spectra of titanium- and aluminum-rich nanolamellae. The volumes ($1 \times 1 \times 25 \text{ nm}^3$) used for the mass spectrum analyses are highlighted by solid lines in (d).

oxygen impurity level (0.1 at.%), the average nitrogen concentration is $50.4 \pm 1.5 \text{ at.}\%$. Similarly, a nitrogen concentration of $49.7 \pm 1.5 \text{ at.}\%$ is obtained for AlN without considering oxygen (1.0 at.%) and argon (0.6 at.%) impurities. Hence, the monolithic films are stoichiometric within the measurement uncertainties. Furthermore, the microstructure has been characterized through STEM and the insets of Fig. 2a and b demonstrate dense, columnar grain morphologies.

Nitrogen contents were also quantified from APT data, employing

the UV as well as the green laser. The pulse energies were varied within a single measurement and corresponding voltage and background evolutions can be found in Figs. S12 and S13 in the Supplementary information. Electric field strengths for different laser pulse energies were obtained from Kingham curves [25] and the electric field strength-dependent nitrogen content is shown in Fig. 2c and d for TiN and AlN, respectively. In case of TiN thin films (Fig. 2c), the electric field strengths were estimated from $\text{Ti}^{2+}/\text{Ti}^{3+}$ charge state ratios and the

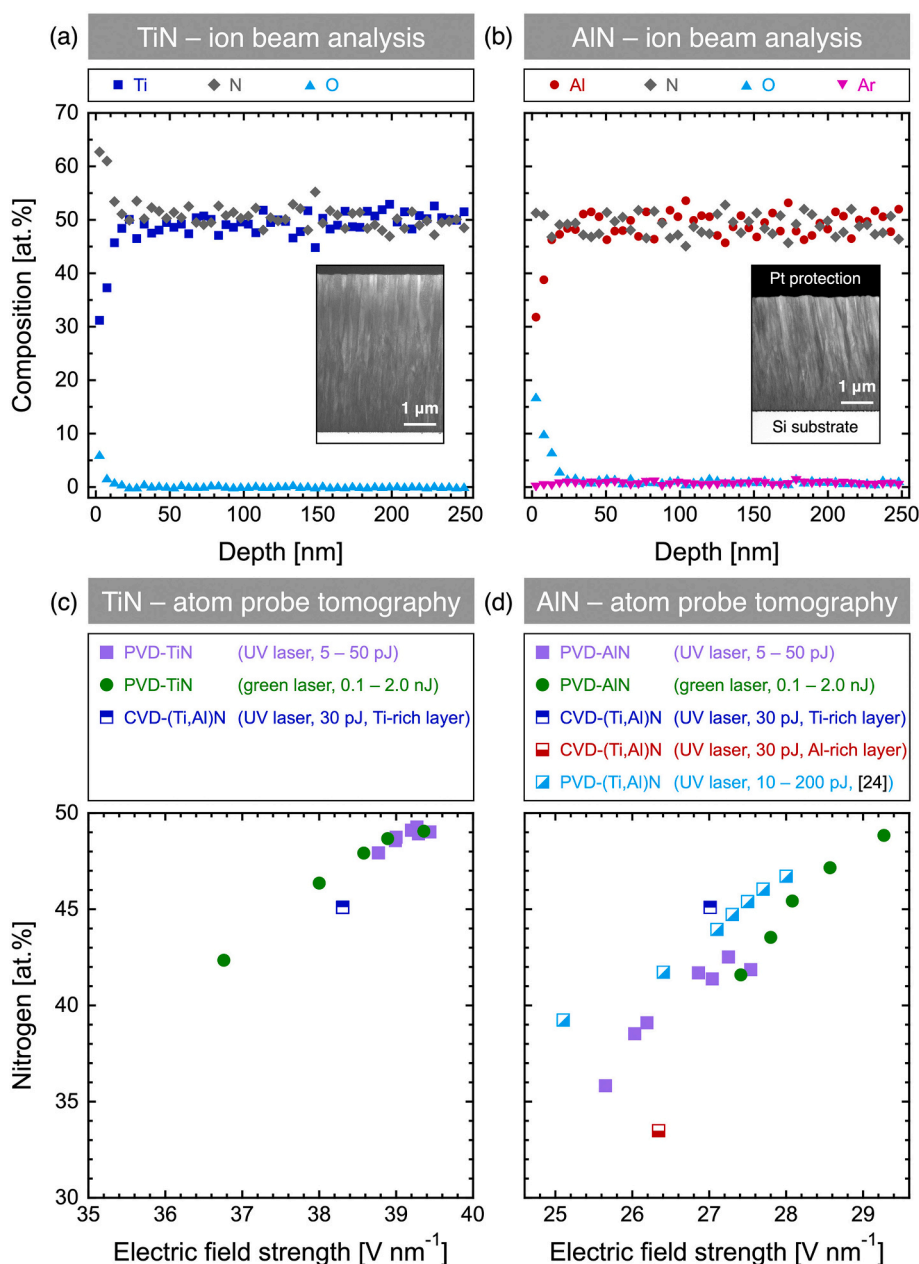


Fig. 2. Comparison of ion beam analysis and atom probe tomography data of monolithic TiN and AlN films. (a) ERDA/RBS depth profile of TiN and the microstructure of the film with a thickness of ~4.9 μm is presented within the inset using STEM. (b) ERDA/RBS depth profile of AlN and the microstructure of the film with a thickness of ~3.6 μm is presented within the inset using STEM. (c) Electric field strength-dependent nitrogen content of TiN, obtained with varying laser pulse energies (UV and green laser) as well as the titanium-rich nanolamella of the CVD-(Ti,Al)N sample (UV laser). (d) Electric field strength-dependent nitrogen content of AlN, obtained with varying laser pulse energies (UV and green laser) as well as the titanium- and aluminum-rich nanolamellae of the CVD-(Ti,Al)N sample (UV laser) and literature data from monolithic c-(Ti,Al)N (UV laser) [24]. Electric field strengths were obtained from $\text{Ti}^{2+}/\text{Ti}^{3+}$ isotope ratios for TiN as well as $\text{Al}^{2+}/\text{Al}^{+}$ isotope ratios for AlN.

decrease from 39.4 to 38.8 V nm⁻¹ for the UV laser (corresponding to an increase of the pulse energy from 5 to 50 pJ) caused a slight reduction of the measured nitrogen content from 49.0 to 47.9 at.%. Decreasing the electric field strength for the green laser from 39.4 to 36.8 V nm⁻¹ (corresponding to an increase of the pulse energy from 0.1 to 2 nJ) was accompanied by a nitrogen reduction from 49.0 to 42.3 at.%. As evident from Fig. 2c, the nitrogen quantification from both APT datasets is in very good agreement and exhibits an almost linear reduction with decreasing electric field strength. Moreover, at minimum laser pulse energies (5 pJ for the UV laser and 0.1 nJ for the green laser) the nitrogen content of 49.0 at.%, measured by APT, is in very good agreement with the 50.4 ± 1.5 at.% nitrogen concentration from ion beam analysis data.

In contrast, the nitrogen quantification of the AlN film depends significantly on the laser type as well as the laser pulse energy (Fig. 2d). Electric field strengths were estimated from $\text{Al}^{2+}/\text{Al}^{+}$ charge state ratios and the decrease of the electric field strength from 27.5 to 25.7 V nm⁻¹ for the UV laser (corresponding to an increase of the pulse energy from 5

to 50 pJ) caused a reduction of the nitrogen content from 41.9 to 35.8 at.%. The dependence of the nitrogen quantification from the electric field strength for the UV laser is consistent with recently published data of AlN, synthesized by metal-organic chemical vapor deposition: nitrogen contents of 42.3 and 36.8 at.% were obtained for $\text{Al}^{2+}/\text{Al}^{+}$ charge state ratios of 6.50 and 0.82 [42], which correspond to electric field strengths of 27.8 and 25.9 V nm⁻¹, respectively. A significantly higher nitrogen content was measured with the green laser. The decrease of the electric field strength from 29.3 to 27.4 V nm⁻¹ (corresponding to an increase of the pulse energy from 0.1 to 2.0 nJ) resulted in a reduction of the nitrogen content from 48.4 to 41.4 at.%.

The here presented datasets on monolithic TiN and AlN thin films illustrate that the influence of the employed laser on the quantification of nitrogen depends strongly on the material system. In case of TiN an electric field strength of 39.4 V nm⁻¹ and a nitrogen content of 49.0 at.% is reached with both lasers, when using pulse energies of 5 pJ (UV laser) and 0.1 nJ (green laser). Hence, a factor ~20 higher laser pulse energy is required in case of the green laser to achieve an electric field strength

comparable to the UV laser. The green and UV laser have different spot sizes (~ 10 and < 5 μm diameter, respectively, determined at the e^{-2} intensity [43]), thus, thermal energy input from the green laser is less efficient due to the larger spot size. An order of magnitude higher laser pulse energy is usually required for the green laser to obtain similar electric field strength as with the UV laser [44]. Experiments on silicon revealed a factor ~ 15 difference of energy input between green and UV laser [45]. However, for AlN films a substantially higher electric field strength of up to 29.3 V nm^{-1} is reached with the green laser at 0.1 nJ , resulting in a nitrogen content of $48.4 \text{ at.}\%$. While the highest electric field strength of 27.5 V nm^{-1} and a nitrogen content of $41.9 \text{ at.}\%$ is obtained with the UV laser at a pulse energy of 5 pJ , a similar electric field strength of 27.4 V nm^{-1} and corresponding nitrogen content of $41.4 \text{ at.}\%$ is found for a pulse energy of 2 nJ with the green laser. Thus, there is a factor ~ 400 difference of energy input between green and UV laser for AlN films, while for TiN this factor is only ~ 20 . These substantial differences in energy input between the UV and green laser for TiN and AlN are obviously material-dependent. While TiN is electrically conductive [46], AlN is a wide bandgap semiconductor [47]. In addition, one order of magnitude difference in thermal conductivity between TiN and AlN has been reported [48]. These properties likely influence the evaporation behavior, when using different laser systems, but are out of scope of this work.

The nitrogen content of the titanium-rich nanolamella (analyzed volume of $1 \times 1 \times 25 \text{ nm}^3$, see Fig. 1d and f) from the CVD-(Ti,Al)N film is also compared to the monolithic TiN films (Fig. 2c). Despite the limited measurement statistics for the titanium-rich nanolamella, its electric field strength and nitrogen content is with 38.2 V nm^{-1} and $45.1 \text{ at.}\%$, respectively, in very good agreement with the electric field strength-dependent nitrogen content of monolithic TiN. Furthermore, the recently published nitrogen contents of PVD-(Ti,Al)N films as a function of electric field strength [24] exhibit a similar evolution as the monolithic AlN films (Fig. 2d). However, the PVD-(Ti,Al)N solid solution films exhibit 2 to 3 at.% higher nitrogen contents than monolithic AlN, which can be understood by the fact that TiN has a higher evaporation field than AlN (Fig. 2c and d). Under the assumption of a linear relationship between nitrogen content and electric field strength, the enhancement of the electric field strength by 1 V nm^{-1} within monolithic TiN, AlN and even c-(Ti,Al)N causes an increase of the measured nitrogen content between 2 and 4 at.%. It appears reasonable that this range of 2 to 4 at.% is affected by both the film material as well as the employed laser.

However, a completely different relationship is obtained, when considering the nitrogen contents and electric field strengths estimated from $\text{Al}^{2+}/\text{Al}^{+}$ charge state ratios for the nanolamellar CVD-(Ti,Al)N film (Fig. 2d). The titanium-rich and aluminum-rich nanolamellae exhibit nitrogen contents of 45.1 and $33.5 \text{ at.}\%$, while the corresponding electric field strengths are 27.0 and 26.3 V nm^{-1} , respectively. Consequently, the transition from the aluminum-rich to the titanium-rich nanolamellae, results in an enhancement of the electric field strength by 0.7 V nm^{-1} and an increase of the measured nitrogen content by $11.6 \text{ at.}\%$, which is substantially larger than the 2 to 4 at.% increase for monolithic films. Thus, it can be learned that changes in electric field strength in nanolamellar CVD-(Ti,Al)N affect the measured nitrogen content more drastically than the laser spot size or the laser wavelength. Next, ion beam analysis and laser-assisted APT data is correlated for a trilayer film, which mimics the modulations in composition of nanolamellar CVD-(Ti,Al)N.

3.3. Correlative compositional analysis of TiN/AlN/TiN trilayer

In order to mimic nanolamellar architectures with defined, straight interfaces for correlative compositional analysis, a TiN/AlN/TiN trilayer with nominal thickness of $\sim 40 \text{ nm}$ per layer was synthesized. The cross-sectional STEM micrograph (Fig. 3) reveals that the TiN layers exhibit a thickness of $33\text{--}34 \text{ nm}$, while the AlN layer thickness is 49 nm . This total

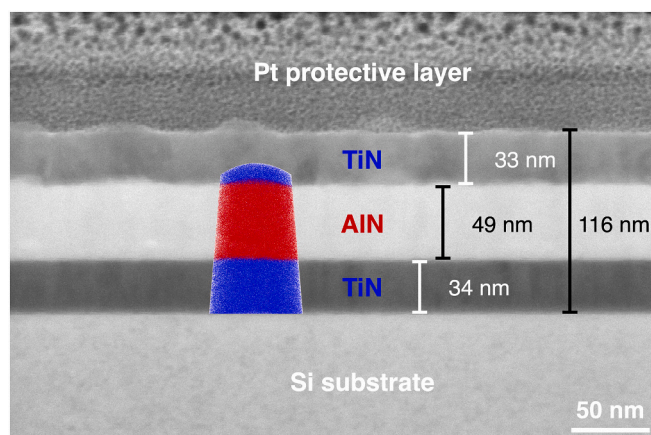


Fig. 3. Cross-sectional micrograph of the TiN/AlN/TiN trilayer architecture with an overlay of the reconstructed volume of titanium and aluminum atomic positions analyzed by atom probe tomography with the UV laser.

thickness of 116 nm is beneficial for the correlative characterization. Both, Rutherford backscattering spectra as well as ToF-ERDA depth profiles are suited to cover the entire TiN/AlN/TiN trilayer. An atom probe reconstruction from a measurement with the UV laser is also included in Fig. 3 as an overlay and it is evident that a reasonable amount of APT data can be collected, including the AlN layer as well as the TiN layer at the film-substrate interface, while the top TiN layer is sacrificed for sharpening of the atom probe specimens.

The compositional characterization of the TiN/AlN/TiN trilayer using laser-assisted APT with the UV as well as the green laser is presented in Fig. 4a and b, respectively. Based on the data of monolithic films a pulse energy of 10 pJ was chosen for the UV laser. While for 5 pJ laser pulse energy the measurement accuracy was slightly higher (nitrogen contents of $49.0 \text{ at.}\%$ at 5 pJ and $48.9 \text{ at.}\%$ at 10 pJ for TiN, Fig. 2c, as well as $41.6 \text{ at.}\%$ at 5 pJ and $41.1 \text{ at.}\%$ at 10 pJ for AlN, Fig. 2d), a lower background was obtained at 10 pJ (7 ppm ns^{-1} at 5 pJ and 5 ppm ns^{-1} at 10 pJ for TiN, Fig. SI2c, as well as 40 ppm ns^{-1} at 5 pJ and 30 ppm ns^{-1} at 10 pJ for AlN, Fig. SI3c). In addition, the measurement stability was enhanced, when using higher laser pulse energy and premature fracture of the specimen at the layer interfaces could be avoided by using 10 pJ . The laser pulse energy of 0.5 nJ was adopted from Qiu et al. [20] for the green laser. The following analyses are focused on the AlN layer as well as the TiN layer at the film-substrate interface.

Consistent with the microstructural analysis (Fig. 3), the reconstructions of atomic positions reveal sharp interfaces. Composition profiles were extracted from cylindrical volumes with 10 nm diameter at the center of the reconstructions. Independent of the employed laser, the oxygen and argon impurities in the AlN layer are 0.6 ± 0.2 and $0.5 \pm 0.2 \text{ at.}\%$, respectively, and the argon content in the TiN layer is $0.2 \pm 0.1 \text{ at.}\%$. Significant oxygen incorporation is visible within the TiN layer and average contents are $5.7 \pm 0.7 \text{ at.}\%$ for the measurement with the UV laser and $7.3 \pm 0.7 \text{ at.}\%$ for the green laser. Since the oxygen content in the AlN layer is significantly lower compared to the TiN layers, despite the higher purity of the titanium target (Kurt J. Lesker, purity 99.995%) than the aluminum target (Kurt J. Lesker, purity 99.99%), it is unlikely that the oxygen originates from the target materials. Instead, a plausible explanation is that titanium acts as a getter material for residual oxygen (or water vapor). As the sputtering process progresses, the effect diminishes, as both targets were continuously operated throughout the deposition process (with only the shutters being opened or closed). Accordingly, a higher oxygen content is observed in the TiN layer at the film-substrate interface than in the top TiN layer (Fig. 4a and b).

The effect of the electric field strength on the measured composition

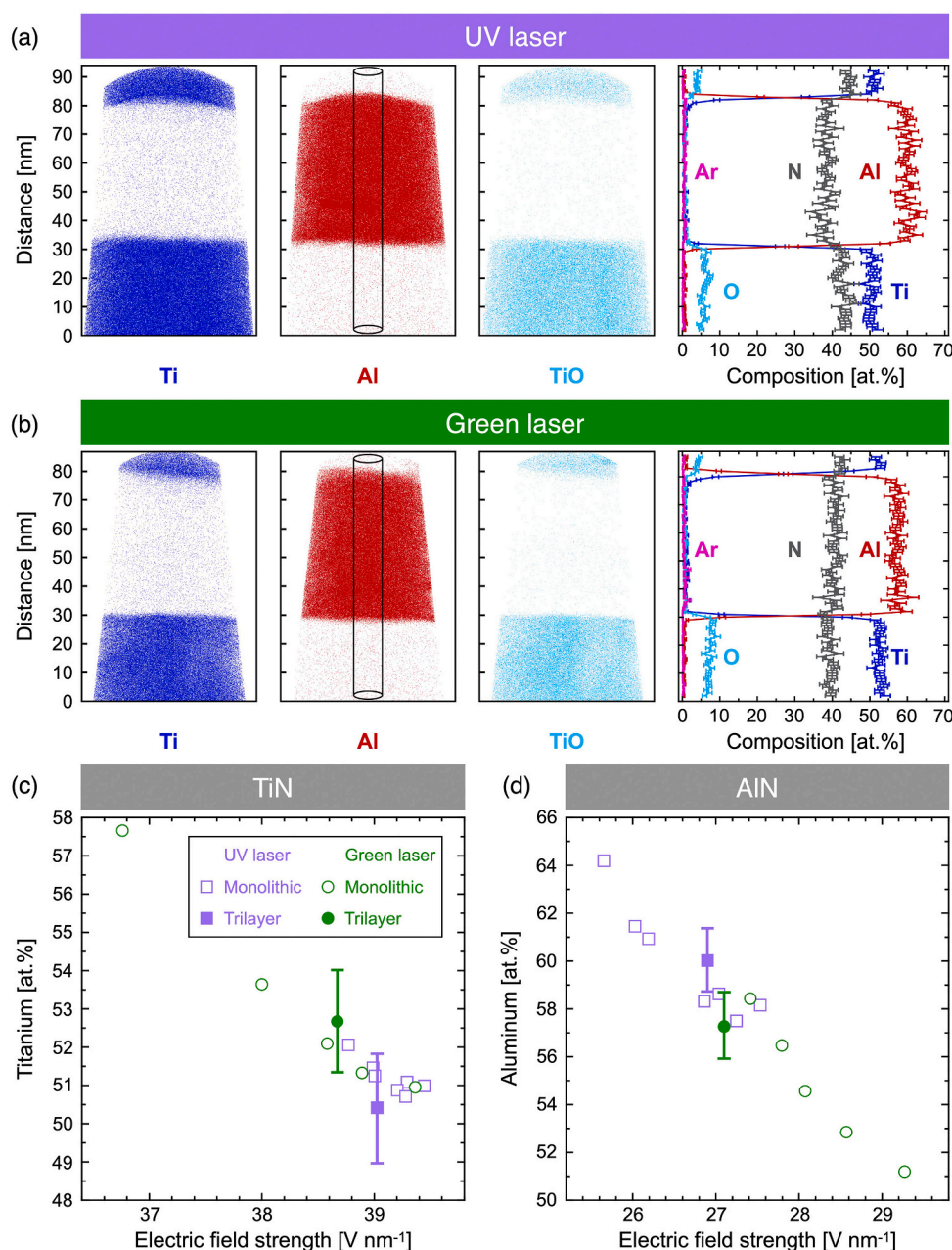


Fig. 4. Atom probe analysis of the TiN/AlN/TiN trilayer architecture using the UV and green laser. (a) Reconstruction of atomic positions of elemental titanium and aluminum ions as well as molecular TiO ions, measured with the UV laser. The composition profile originates from the cylindrical volume with 10 nm diameter. (b) Reconstruction of atomic positions of elemental titanium and aluminum ions as well as molecular TiO ions, measured with the green laser. The composition profile originates from the cylindrical volume with 10 nm diameter. The distance of 0 nm corresponds to the film-substrate interface in both composition profiles. (c) Comparison of the electric field strength-dependent titanium content of the TiN/AlN/TiN trilayer (TiN layer at the film-substrate interface) to monolithic TiN films. (d) Comparison of the electric field strength-dependent aluminum content of the TiN/AlN/TiN trilayer (AlN layer) to monolithic AlN films. Electric field strengths were obtained from $\text{Ti}^{2+}/\text{Ti}^{3+}$ isotope ratios for TiN as well as $\text{Al}^{2+}/\text{Al}^{3+}$ isotope ratios for AlN. The legend provided in (c) is also valid for (d).

of the TiN/AlN/TiN trilayer is compared to monolithic TiN and AlN films in Fig. 4c and d, respectively. The electric field strength-composition data of the monolithic films is identical to Fig. 2c and d, but due to the significant oxygen incorporation in the TiN layers of the trilayer, the metal contents are plotted in Fig. 4c and d. Titanium and nitrogen contents of the TiN layer at the film-substrate interface of the trilayer are 50 ± 1 as well as 43 ± 1 at.% for the UV laser (Fig. 4a) and 53 ± 1 as well as 39 ± 1 at.% for the green laser (Fig. 4b), respectively. Despite the presence of oxygen impurities, the electric field strength and composition of the TiN layer is in good agreement with the monolithic TiN films (Fig. 4c), when considering the precision of laser-assisted APT on the order of ± 1 at.% for both instruments (error bars in Fig. 4c and d were obtained from the cylindrical composition profiles in Fig. 4a and b). The higher nitrogen content of 43 ± 1 at.% for the UV laser compared to 39 ± 1 at.% for the green laser is consistent with the electric field strengths of 39.0 and 38.7 V nm⁻¹, respectively. The electric field strength and composition of the AlN layer is also in good

agreement with the monolithic AlN films (Fig. 4d). Aluminum and nitrogen contents of the AlN layer are 60 ± 1 as well as 38 ± 1 at.% for the UV laser (Fig. 4a) and 57 ± 1 as well as 41 ± 1 at.% for the green laser (Fig. 4b), respectively. The corresponding electric field strengths are 26.9 V nm⁻¹ for the UV laser and 27.1 V nm⁻¹ for the green laser. Hence, the measured nitrogen content is increased due to the larger electric field strength in case of the green laser.

The identical TiN/AlN/TiN trilayer film has been characterized by ion beam analysis as presented in Fig. 5. The three individual layers can be identified from the Rutherford backscattering spectrum, i.e. two individual titanium contributions in the energy range of ~ 1.30 to ~ 1.45 MeV as well as aluminum at ~ 1.05 MeV, Fig. 5a. Moreover, argon, oxygen and nitrogen were considered and the best fit is obtained with 49 at.% titanium, 46 at.% nitrogen as well as 5 at.% oxygen for the TiN top layer, while the TiN layer at the film-substrate interface exhibits concentrations of 48 at.% titanium, 45 at.% nitrogen and 7 at.% oxygen. The composition of the AlN layer is close to the 1:1 stoichiometry with

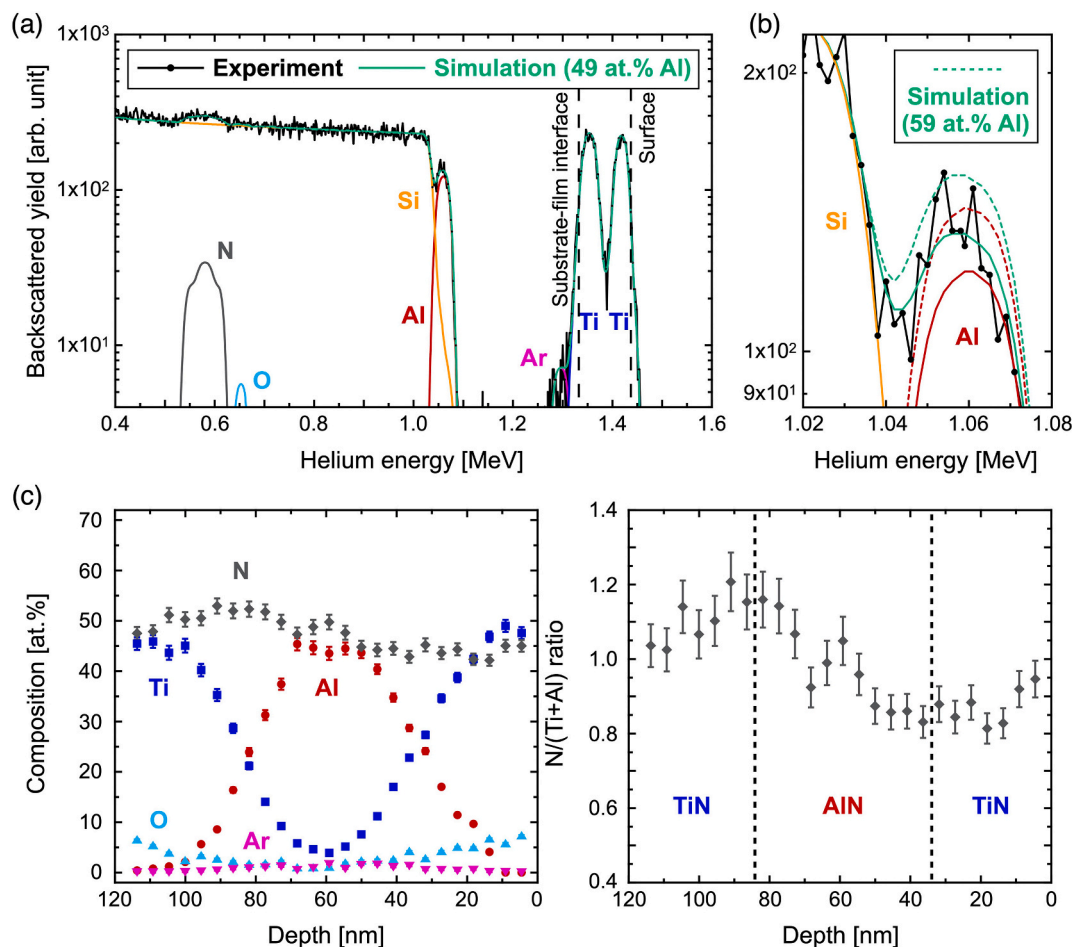


Fig. 5. Ion beam analysis of the TiN/AlN/TiN trilayer architecture. (a) Rutherford backscattering spectrum. (b) Magnification of the aluminum signal with two sets of simulations: 49 at.% aluminum (best fit, solid lines) and 59 at.% aluminum (dashed lines). (c) ToF-ERDA depth profile of the elemental concentrations as well as the N/(Ti+Al) ratio. The depth was calibrated with thickness measurements from STEM (see Fig. 3) and 0 nm corresponds to the film–substrate interface.

49 at.% aluminum, 50 at.% nitrogen as well as 1 at.% argon. Since the nitrogen content of the AlN layer has been quantified in the range of 38 ± 1 to 41 ± 1 at.% based on APT data (Fig. 4), two simulations with 49 and 59 at.% aluminum are additionally compared in Fig. 5b. It is obvious that the fit from the simulation with 59 at.% aluminum represents an overestimation with respect to the experimental data.

The depth profile, obtained by ToF-ERDA (Fig. 5c), is within the measurement uncertainties ($< \pm 2$ at.% for nitrogen) in good agreement with the RBS data. Average concentrations of 46 at.% titanium, 48 at.% nitrogen and 6 at.% oxygen are obtained for the TiN top layer. The AlN layer exhibits 47 at.% aluminum, 51 at.% nitrogen as well as 1 at.% argon and 1 at.% oxygen. In case of the TiN layer at the film–substrate interface, average concentrations of 48 at.% titanium, 45 at.% nitrogen and 7 at.% oxygen are quantified. Consequently, the N/(Ti+Al) ratio of the individual layers is in the range of 0.9 to 1.1, while at the interfaces (indicated with dashed lines in Fig. 5c) the variations are larger in the range of 0.8 to 1.2.

Finally, composition data obtained from ion beam analysis (Fig. 5) as well as laser-assisted APT (Fig. 4) is correlated in Fig. 6a and b for the UV and green laser, respectively. Significant deviations with respect to the nitrogen content are observed for the AlN layer. While the average nitrogen concentration from ion beam analysis is 51 at.%, the nitrogen content from laser-assisted APT data is only 38 at.% for experiments with the UV laser (Fig. 6a) or 41 at.% in case of the green laser (Fig. 6b). Hence, the nitrogen content of the AlN layer is underestimated from laser-assisted APT data by at least 10 and up to 13 at.%. This significant discrepancy cannot be explained by the measurement uncertainties,

which are $< \pm 2$ at.% for APT data and $< \pm 2$ at.% for individual data points in ToF-ERDA depth profiles.

In contrast, the composition data from ion beam analysis and laser-assisted APT of the TiN layer is in very good agreement for the dataset measured with the UV laser (Fig. 6a). The composition of 48 at.% titanium, 45 at.% nitrogen and 7 at.% oxygen has been obtained by ion beam analysis, while laser-assisted APT data consistently resulted in 50 at.% titanium, 43 at.% nitrogen and 7 at.% oxygen. Hence, in case of the TiN layer the compositional deviations of titanium and nitrogen are within the measurement uncertainties of both techniques. Larger deviations can be observed for the dataset measured with the green laser (Fig. 6b), since 53 at.% titanium, 39 at.% nitrogen and 8 at.% oxygen were obtained. The lower nitrogen content (39 at.%) in comparison to the dataset measured with the UV laser (43 at.%) is a consequence of the relatively high laser pulse energy of 0.5 nJ. Based on the electric field strength-dependent nitrogen content, presented in Figs. 2c and 4c, it is reasonable to assume that a lower pulse energy of the green laser (such as 0.1 nJ) would cause a higher electric field strength and consequently yield consistent composition data with the UV laser pulse energy of 10 pJ for analysis of TiN.

In summary, this work clearly demonstrates the limited measurement accuracy of laser-assisted APT, which depends substantially on the electric field strength. Correlation of compositions from ion beam analysis and laser-assisted APT data for the TiN/AlN/TiN trilayer film revealed that underestimation of nitrogen for aluminum-rich volumes has to be expected to an extent of 10 to 13 at.%. While in case of titanium-rich volumes reasonable measurement accuracy has been

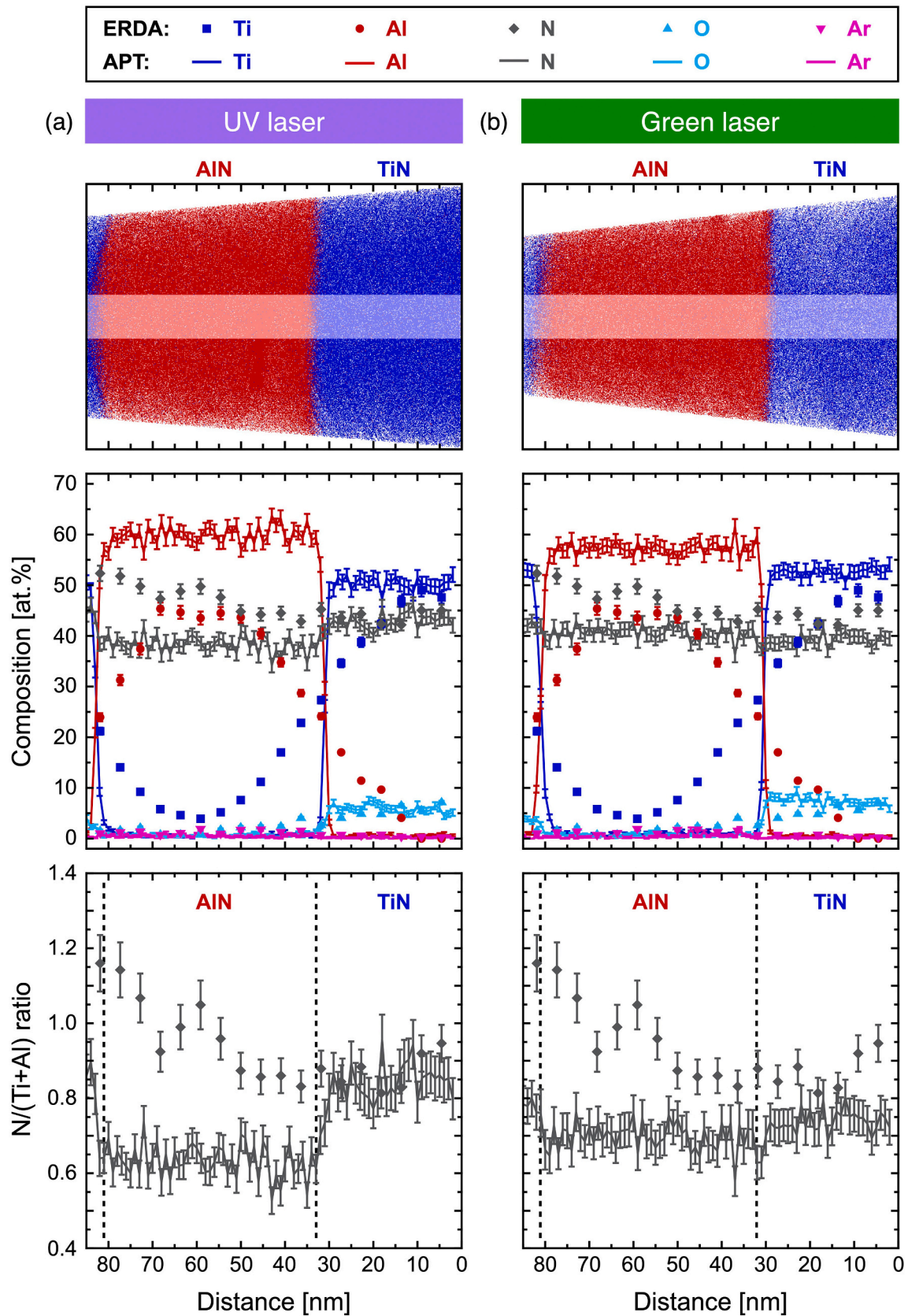


Fig. 6. Comparison of ion beam analysis and atom probe tomography data of the TiN/AlN/TiN trilayer architecture. Atom probe data has been obtained with the (a) UV and (b) green laser. Ion beam analysis data is shown with data points, while compositions measured with the atom probes are presented with solid lines. The distance of 0 nm corresponds to the film–substrate interface in all profiles.

obtained with the UV laser pulse energy of 10 pJ, it is evident that the laser pulse energy is a critical parameter, which governs the electric field strength. Therefore, underestimation of the nitrogen content can also occur for titanium-rich volumes as the observed 4 at.% with the green laser at a pulse energy of 0.5 nJ.

The strong underestimation of nitrogen for aluminum-rich volumes is caused by the relatively low evaporation field ($<30 \text{ V nm}^{-1}$ for AlN, Fig. 4d) compared to titanium-rich volumes ($>36 \text{ V nm}^{-1}$ for TiN, Fig. 4c). For GaN it has been demonstrated that dissociation of nitrogen-containing molecular ions occurs, causing the formation of neutral fragments [16]. The mass spectra of the here investigated samples (Fig. 1f, Figs. S14 to S129) exhibit e.g. pronounced fractions of molecular N_2^+ ions at 28 Da, hence, dissociation thereof results in neutral nitrogen fragments, which are not detected. In case of aluminum-rich volumes the low electric field strength appears to be insufficient for ionization of these neutral fragments. Therefore, strong underestimation of nitrogen is observed for both monolithic AlN as well as the AlN layer in the trilayer film and it is reasonable to expect similar effects in nanolamellar (Ti,Al)N.

Consequently, the interpretation of 36 % nitrogen vacancies in aluminum-rich volumes as well as 12 % metal vacancies in titanium-rich volumes of nanolamellar (Ti,Al)N proposed by Qiu et al. originates from the limited measurement accuracy of APT, induced by the electric field strength. While it appears reasonable that metal and nitrogen vacancies govern nitrogen overstoichiometry and understoichiometry, the here presented correlative ion beam analysis and APT data unequivocally prove that the quantification of vacancy concentrations in nanolamellar (Ti,Al)N thin films solely based on atom probe data is not meaningful. In order to draw scientifically sound conclusions, complementary characterization techniques are essential as the measurement accuracy of APT – or lack thereof – critically depends on the field evaporation conditions [24].

4. Conclusions

Motivated by the recent APT-based quantification of vacancy concentrations for a CVD-(Ti,Al)N film with nanolamellar architecture [20], we have systematically compared laser-assisted APT measurements with a UV as well as a green laser to ion beam analysis data for this material system.

First, a CVD-(Ti,Al)N film was measured by APT with a UV laser and titanium- and aluminum-rich nanolamellae exhibited average nitrogen contents of 42 ± 4 and 34 ± 3 at.%, respectively. A systematic comparison of nitrogen quantification from laser-assisted APT with the UV and green laser has been carried out for monolithic TiN and AlN films, which were stoichiometric within the measurement uncertainties of ion beam analysis. In case of TiN an electric field strength of 39.4 V nm^{-1} and a nitrogen content of 49.0 at.%, consistent with ion beam analysis data, was obtained with both lasers, when using pulse energies of 5 pJ (UV laser) and 0.1 nJ (green laser). However, significant differences were observed for monolithic AlN as nitrogen contents from 41.9 to 35.8 at.% and 48.4 to 41.4 at.% were measured, depending on variations of the pulse energies of the UV and green laser, respectively. Moreover, electric field strengths extracted from the nanolamellae of the CVD-(Ti,Al)N film revealed that changes of the electric field strength affect the measured nitrogen content more drastically than the laser spot size or the laser wavelength.

In order to mimic a nanolamellar architecture with defined, straight interfaces for correlative compositional analysis by ion beam analysis and laser-assisted APT, a TiN/AlN/TiN trilayer film was synthesized. Significant deviations with respect to the nitrogen content were evident for the AlN layer. While the average nitrogen concentration from ion beam analysis was 51 at.%, nitrogen contents from laser-assisted APT data were only 38 at.% (UV laser) or 41 at.% (green laser). Hence, the nitrogen content of the AlN layer is underestimated from laser-assisted APT data by at least 10 and up to 13 at.% and this significant discrepancy cannot be

explained by the measurement uncertainties. In case of the TiN layer reasonable agreement has been obtained between ion beam analysis and APT data with the UV laser at 10 pJ laser pulse energy. In contrast, the nitrogen content was underestimated by 4 at.% in case of the green laser due to the relatively high pulse energy of 0.5 nJ.

Thus, the here presented correlative ion beam analysis and APT data unequivocally prove that the quantification of vacancy concentrations in nanolamellar (Ti,Al)N thin films solely based on atom probe data is not meaningful. In order to draw scientifically sound conclusions, complementary characterization techniques are essential as the measurement accuracy of APT – or lack thereof – critically depends on the field evaporation conditions [24].

CRediT authorship contribution statement

Marcus Hans: Conceptualization, Formal analysis, Funding acquisition, Investigation, Methodology, Writing – original draft. **Michael Tkadletz:** Conceptualization, Formal analysis, Investigation, Methodology, Writing – review & editing. **Daniel Primetzhofer:** Conceptualization, Formal analysis, Investigation, Methodology, Writing – review & editing. **Helene Waldl:** Formal analysis, Investigation, Writing – review & editing. **Maximilian Schiester:** Formal analysis, Investigation, Writing – review & editing. **Matthias Bartosik:** Formal analysis, Funding acquisition, Investigation, Methodology, Writing – review & editing. **Christoph Czettel:** Funding acquisition, Methodology, Writing – review & editing. **Nina Schalk:** Funding acquisition, Supervision, Writing – review & editing. **Christian Mitterer:** Funding acquisition, Supervision, Writing – review & editing. **Jochen M. Schneider:** Funding acquisition, Supervision, Writing – review & editing.

Declaration of competing interest

The authors declare that they have no known competing financial interests or personal relationships that could have appeared to influence the work reported in this paper.

Data availability

Data will be made available on request.

Acknowledgments

This research was funded by Deutsche Forschungsgemeinschaft (DFG) within the project 515702322 (HA 9139/1-1, SCHN 735/50-1). Transnational access for ion beam analysis at Uppsala University has been supported by the RADIATE project under the Grant Agreement 824096 from the EU Research and Innovation programme HORIZON 2020. Accelerator operation at Uppsala University has been supported by the Swedish Research Council VR-RFI (#2019.00191). Matthias Bartosik acknowledges financial support from the Austrian Science Fund (FWF): I-4720.

Appendix A. Supplementary data

Supplementary data to this article can be found online at <https://doi.org/10.1016/j.surfcoat.2023.130020>.

References

- [1] A. Hörling, L. Hultman, M. Odén, J. Sjölen, L. Karlsson, Thermal stability of arc evaporated high aluminum-content $\text{Ti}_{1-x}\text{Al}_x\text{N}$ thin films, *J. Vac. Sci. Technol. A* 20 (2002) 1815–1823, <https://doi.org/10.1116/1.1503784>.
- [2] P.H. Mayrhofer, A. Hörling, L. Karlsson, J. Sjölen, T. Larsson, C. Mitterer, L. Hultman, Self-organized nanostructures in the Ti–Al–N system, *Appl. Phys. Lett.* 83 (2003) 2049–2051, <https://doi.org/10.1063/1.1608464>.
- [3] M. Hans, H. Rueß, Z. Czigány, J. Krause, P. Ondračka, D. Music, S. Evertz, D. M. Holzapfel, D. Primetzhofer, J.M. Schneider, Spinodal decomposition of

- reactively sputtered ($\text{V}_{0.64}\text{Al}_{0.36}\text{O}_{0.49}\text{N}_{0.51}$) thin films, *Surf. Coat. Technol.* 389 (2020), 125641, <https://doi.org/10.1016/j.surfcoat.2020.125641>.
- [4] M. Hans, Z. Czigány, D. Neuß, J.A. Sälker, H. Rueß, J. Krause, G.K. Nayak, D. Holec, J.M. Schneider, Probing the onset of wurtzite phase formation in (V,Al)N thin films by transmission electron microscopy and atom probe tomography, *Surf. Coat. Technol.* 442 (2022), 128235, <https://doi.org/10.1016/j.surfcoat.2022.128235>.
- [5] R. Rachbauer, E. Stergar, S. Massl, M. Moser, P.H. Mayrhofer, Three-dimensional atom probe investigations of Ti–Al–N thin films, *Scr. Mater.* 61 (2009) 725–728, <https://doi.org/10.1016/j.scriptamat.2009.06.015>.
- [6] E.W. Müller, Field desorption, *Phys. Rev.* 102 (1956) 618–624, <https://doi.org/10.1103/PhysRev.102.618>.
- [7] B. Gault, F. Vurpillot, A. Vella, M. Gilbert, A. Menand, D. Blavette, B. Deconihout, Design of a femtosecond laser assisted tomographic atom probe, *Rev. Sci. Instrum.* 77 (2006), 043705, <https://doi.org/10.1063/1.2194089>.
- [8] R. Haydock, D.R. Kingham, Post-ionization of field-evaporated ions, *Phys. Rev. Lett.* 44 (1980) 1520–1523, <https://doi.org/10.1103/PhysRevLett.44.1520>.
- [9] G. Greczynski, L. Hultman, Compromising science by ignorant instrument calibration—need to revisit half a century of published XPS data, *Angew. Chem. Int. Ed.* 59 (2020) 5002–5006, <https://doi.org/10.1002/anie.201916000>.
- [10] F. De Geuser, B. Gault, Metrology of small particles and solute clusters by atom probe tomography, *Acta Mater.* 188 (2020) 406–415, <https://doi.org/10.1016/j.actamat.2020.02.023>.
- [11] B. Gault, B. Klaes, F.F. Morgado, C. Freysoldt, Y. Li, F. De Geuser, L.T. Stephenson, F. Vurpillot, Reflections on the spatial performance of atom probe tomography in the analysis of atomic neighborhoods, *Microsc. Microanal.* (2021), <https://doi.org/10.1017/S1431927621012952>.
- [12] R. Agrawal, R.A. Bernal, D. Isheim, H.D. Espinosa, Characterizing atomic composition and dopant distribution in wide band gap semiconductor nanowires using laser-assisted atom probe tomography, *J. Phys. Chem. C* 115 (2011) 17688–17694, <https://doi.org/10.1021/jp2047823>.
- [13] J.R. Riley, R.A. Bernal, Q. Li, H.D. Espinosa, G.T. Wang, L.J. Lauhon, Atom probe tomography of α -axis GaN nanowires: analysis of nonstoichiometric evaporation behavior, *ACS Nano* 6 (2012) 3898–3906, <https://doi.org/10.1021/nn2050517>.
- [14] D.R. Diercks, B.P. Gorman, R. Kirchhofer, N. Sanford, K. Bertness, M. Brubaker, Atom probe tomography evaporation behavior of C-axis GaN nanowires: crystallographic, stoichiometric, and detection efficiency aspects, *J. Appl. Phys.* 114 (2013), 184903, <https://doi.org/10.1063/1.4830023>.
- [15] L. Mancini, N. Amirifar, D. Shinde, I. Blum, M. Gilbert, A. Vella, F. Vurpillot, W. Lefebvre, R. Lardé, E. Talbot, P. Pareige, X. Portier, A. Ziani, C. Davesne, C. Durand, J. Eymery, R. Butte, J.-F. Carlin, N. Grandjean, L. Rigutti, Composition of wide bandgap semiconductor materials and nanostructures measured by atom probe tomography and its dependence on the surface electric field, *J. Phys. Chem. C* 118 (2014) 24136–24151, <https://doi.org/10.1021/jp5071264>.
- [16] B. Gault, D.W. Saxey, M.W. Ashton, S.B. Sinnott, A.N. Chiamanti, M.P. Moody, D. K. Schreiber, Behavior of molecules and molecular ions near a field emitter, *New J. Phys.* 18 (2016), 033031, <https://doi.org/10.1088/1367-2630/18/3/033031>.
- [17] E. Di Russo, I. Blum, J. Houard, M. Gilbert, G. Da Costa, D. Blavette, L. Rigutti, Compositional accuracy of atom probe tomography measurements in GaN: impact of experimental parameters and multiple evaporation events, *Ultramicroscopy* 187 (2018) 126–134, <https://doi.org/10.1016/j.ultramic.2018.02.001>.
- [18] R.J.H. Morris, R. Cuduvally, D. Melkonyan, C. Fleischmann, M. Zhao, L. Arnoldi, P. van der Heide, W. Vandervorst, Toward accurate composition analysis of GaN and AlGaN using atom probe tomography, *J. Vac. Sci. Technol. B* 36 (2018), 03F130, <https://doi.org/10.1116/1.5019693>.
- [19] R.J.H. Morris, R. Cuduvally, D. Melkonyan, M. Zhao, P. van der Heide, W. Vandervorst, Atom probe of GaN/AlGaN heterostructures: the role of electric field, sample crystallography and laser excitation on quantification, *Ultramicroscopy* 206 (2019), 112813, <https://doi.org/10.1016/j.ultramic.2019.112813>.
- [20] R. Qiu, H. Aboulfadl, O. Bäcke, D. Stiens, H.-O. André, M. Halvarsson, Atom probe tomography investigation of 3D nanoscale compositional variations in CVD TiAlN nanolamella coatings, *Surf. Coat. Technol.* 426 (2021), 127741, <https://doi.org/10.1016/j.surfcoat.2021.127741>.
- [21] M. to Baben, L. Raumann, D. Music, J.M. Schneider, Origin of the nitrogen over- and understoichiometry in $\text{Ti}_{0.5}\text{Al}_{0.5}\text{N}$ thin films, *J. Phys. Condens. Matter* 24 (2012), 155401, <https://doi.org/10.1088/0953-8984/24/15/155401>.
- [22] B. Alling, A. Karimi, L. Hultman, I.A. Abrikosov, First-principles study of the effect of nitrogen vacancies on the decomposition pattern in cubic $\text{Ti}_{1-x}\text{Al}_x\text{N}_{1-y}$, *Appl. Phys. Lett.* 92 (2008), 071903, <https://doi.org/10.1063/1.2838747>.
- [23] M. to Baben, M. Hans, D. Primetzhofer, S. Evertz, H. Ruess, J.M. Schneider, Unprecedented thermal stability of inherently metastable titanium aluminum nitride by point defect engineering, *Mater. Res. Lett.* 5 (2017) 158–169, <https://doi.org/10.1080/21663831.2016.1233914>.
- [24] M. Hans, J.M. Schneider, Electric field strength-dependent accuracy of TiAlN thin film composition measurements by laser-assisted atom probe tomography, *New J. Phys.* 22 (2020), 033036, <https://doi.org/10.1088/1367-2630/ab7770>.
- [25] D.R. Kingham, The post-ionization of field evaporated ions: a theoretical explanation of multiple charge states, *Surf. Sci.* 116 (1982) 273–301, [https://doi.org/10.1016/0039-6028\(82\)90434-4](https://doi.org/10.1016/0039-6028(82)90434-4).
- [26] M. Hans, J.M. Schneider, On the chemical composition of TiAlN thin films - comparison of ion beam analysis and laser-assisted atom probe tomography with varying laser pulse energy, *Thin Solid Films* 688 (2019) 137251, <https://doi.org/10.1016/j.tsf.2019.04.026>.
- [27] R. Rachbauer, S. Massl, E. Stergar, P. Felfel, P.H. Mayrhofer, Atom probe specimen preparation and 3D interfacial study of Ti–Al–N thin films, *Surf. Coat. Technol.* 204 (2010) 1811–1816, <https://doi.org/10.1016/j.surfcoat.2009.11.020>.
- [28] I. Povstugar, P.-P. Choi, D. Tytko, J.-P. Ahn, D. Raabe, Interface-directed spinodal decomposition in TiAlN/CrN multilayer hard coatings studied by atom probe tomography, *Acta Mater.* 61 (2013) 734–7542, <https://doi.org/10.1016/j.actamat.2013.08.028>.
- [29] S. Liu, K. Chang, S. Mráz, X. Chen, M. Hans, D. Music, D. Primetzhofer, J. M. Schneider, Modeling of metastable phase formation for sputtered $\text{Ti}_{1-x}\text{Al}_x\text{N}$ thin films, *Acta Mater.* 165 (2019) 615–625, <https://doi.org/10.1016/j.actamat.2018.12.004>.
- [30] D.M. Holzapfel, Z. Czigány, A.O. Eriksson, M. Arndt, J.M. Schneider, Thermal stability of macroparticles in $\text{Ti}_{0.27}\text{Al}_{0.21}\text{N}_{0.52}$ coatings, *Appl. Surf. Sci.* 553 (2021), 149527, <https://doi.org/10.1016/j.apsusc.2021.149527>.
- [31] D.M. Holzapfel, D. Music, M. Hans, S. Wolff-Goodrich, D. Holec, D. Bogdanovski, M. Arndt, A.O. Eriksson, K. Yalamanchili, D. Primetzhofer, C.H. Liebscher, J. M. Schneider, Enhanced thermal stability of (Ti,Al)N coatings by oxygen incorporation, *Acta Mater.* 218 (2021), 117204, <https://doi.org/10.1016/j.actamat.2021.117204>.
- [32] A. Kretschmer, D. Holec, K. Yalamanchili, H. Rudigier, M. Hans, J.M. Schneider, P. H. Mayrhofer, Strain-stabilized Al-containing high-entropy sublattice nitrides, *Acta Mater.* 224 (2022), 117483, <https://doi.org/10.1016/j.actamat.2021.117483>.
- [33] C. Saringer, M. Tkadletz, J. Thurner, C. Czetti, N. Schalk, Influence of the deposition parameters on the nanolamella periodicity of chemical vapor deposited $\text{Ti}_{1-x}\text{Al}_x\text{N}$, *Mater. Lett.* 305 (2021), 130819, <https://doi.org/10.1016/j.matlet.2021.130819>.
- [34] P. Ström, D. Primetzhofer, Ion beam tools for nondestructive in-situ and in-operando composition analysis and modification of materials at the Tandem Laboratory in Uppsala, *J. Instrum.* 17 (2022), P04011, <https://doi.org/10.1088/1748-0221/17/04/P04011>.
- [35] P. Ström, P. Petersson, M. Rubel, G. Possnert, A combined segmented anode gas ionization chamber and time-of-flight detector for heavy ion elastic recoil detection analysis, *Rev. Sci. Instrum.* 87 (2016), 103303, <https://doi.org/10.1063/1.4963709>.
- [36] Y. Zhang, H.J. Whitlow, T. Winzell, I.F. Bubb, T. Sajavaara, K. Arstila, J. Keinonen, Detection efficiency of time-of-flight energy elastic recoil detection analysis systems, *Nucl. Inst. Methods Phys. Res. B* 149 (1999) 477–489, [https://doi.org/10.1016/S0168-583X\(98\)00963-X](https://doi.org/10.1016/S0168-583X(98)00963-X).
- [37] M.V. Moro, B. Bruckner, P.L. Grande, M.H. Taabniks, P. Bauer, D. Primetzhofer, Stopping cross section of vanadium for H^+ and He^+ ions in a large energy interval deduced from backscattering spectra, *Nucl. Inst. Methods Phys. Res. B* 424 (2018) 43–51, <https://doi.org/10.1016/j.nimb.2018.03.032>.
- [38] M.S. Janson, *CONTES Instruction Manual, Internal Report, Uppsala, 2004*.
- [39] M. Mayer, SIMNRA, a simulation program for the analysis of NRA, RBS and ERDA, *AIP Conf. Proc.* 475 (1999) 541–544, <https://doi.org/10.1063/1.59188>.
- [40] K. Thompson, D. Lawrence, D.J. Larson, J.D. Olson, T.F. Kelly, B. Gorman, In situ site-specific specimen preparation for atom probe, *Ultramicroscopy* 107 (2007) 131–139, <https://doi.org/10.1016/j.ultramic.2006.06.008>.
- [41] M. Hans, P. Keuter, A. Saksena, J.A. Sälker, M. Momma, H. Springer, J. Nowak, D. Zander, D. Primetzhofer, J.M. Schneider, Opportunities of combinatorial thin film materials design for the sustainable development of magnesium-based alloys, *Sci. Rep.* 11 (2021) 17454, <https://doi.org/10.1038/s41598-021-97036-6>.
- [42] R.J.H. Morris, R. Cuduvally, J.-R. Lin, M. Zhao, W. Vandervorst, M. Thuvander, C. Fleischmann, Field dependent study on the impact of co-evaporated multilayers and ion pile-up for the apparent stoichiometric quantification of GaN and AlN, *Ultramicroscopy* 241 (2022), 113592, <https://doi.org/10.1016/j.ultramic.2022.113592>.
- [43] Y. Amouyal, D.N. Seidman, Atom probe tomography of nickel-based superalloys with green or ultraviolet lasers: a comparative study, *Microsc. Microanal.* 18 (2012) 971–981, <https://doi.org/10.1017/S1431927612001183>.
- [44] T.L. Martin, A.J. London, B. Jenkins, S.E. Hopkin, J.O. Douglas, P.D. Styman, P.A. J. Bagot, M.P. Moody, Comparing the consistency of atom probe tomography measurements of small-scale segregation and clustering between the LEAP 3000 and LEAP 5000 instruments, *Microsc. Microanal.* 23 (2017) 227–237, <https://doi.org/10.1017/S1431927617000356>.
- [45] D. Santhanagopalan, D.K. Schreiber, D.E. Perea, R.L. Martens, Y. Janssen, P. Khalifah, Y.S. Meng, Effects of laser energy and wavelength on the analysis of LiFePO_4 using laser assisted atom probe tomography, *Ultramicroscopy* 148 (2015) 57–66, <https://doi.org/10.1016/j.ultramic.2014.09.004>.
- [46] P. Patsalas, S. Logothetidis, Optical, electronic, and transport properties of nanocrystalline titanium nitride thin films, *J. Appl. Phys.* 90 (2001) 4725–4734, <https://doi.org/10.1063/1.1403677>.
- [47] P.B. Perry, R.F. Rutz, The optical absorption edge of single-crystal AlN prepared by a close-spaced vapor process, *Appl. Phys. Lett.* 33 (1978) 319–321, <https://doi.org/10.1063/1.90354>.
- [48] V. Moraes, H. Riedl, R. Rachbauer, S. Kolozsvári, M. Ikeda, L. Prochaska, S. Paschen, P.H. Mayrhofer, Thermal conductivity and mechanical properties of AlN-based thin films, *J. Appl. Phys.* 119 (2016), 225304, <https://doi.org/10.1063/1.4953358>.